Fast Characterization Of In-Orbit Fragmentations

Gisolfi, L.; Rossi, A.; Marzari, F.

Important note
To cite this publication, please use the final published version (if applicable).
Please check the document version above.

IAC-24,A6,7,x85251

Fast Characterization Of In-Orbit Fragmentations

L. Gisolfi[a,c], A. Rossi[b]*, F. Marzari[c]

[a] *Delft University of Technology, Faculty of Aerospace Engineering, Delft, The Netherlands,* l.gisolfi@tudelft.nl
[b] *IFAC-CNR, Via Madonna del Piano 10, 50019 Sesto Fiorentino (FI), Italy,* a.rossi@ifac.cnr.it
[c] *Università di Padova, Dipartimento di Fisica e Astronomia, Padova, Italy* francesco.marzari@pd.infn.it

* Corresponding Author

Abstract

Building on the definition of the Criticality of Spacecraft Index [1] and of the Shell Criticality [3], a procedure and an index able to quantify and visualize the medium term effects on the environment of a fragmentation in Low Earth Orbit is derived. The index takes into account the change in the environment caused by the fragmentation of a given mass in a specific orbit by quantifying the contribution of the fragments with respect to the original situation where the whole fragmented mass was contained in the intact objects.

The index is devised in the frame of added-value SST services, such as the fragmentation detection and impact evaluation service. Thus, weighting factors are included in its formulation to highlight the contribution of the debris created in a given event, leveraged by the capabilities of a given observing network (either optical or radar).

The index is applied and tested on a few simulated fragmentations. The results show that the index is able to characterize the perturbation to the environment due to the cloud of fragments and its temporal evolution. In particular, the new weighting factors are able to properly highlight the capability of a given SST network to observe and characterize a fragmentation happening in a Low Earth Orbit region.

Keywords: Space surveillance; fragmentation; environmental index.

1. Introduction

Given the rapid expansion of the space activities calling for the so-called Space Traffic Management and the growing need for efficient space surveillance systems , indexes able to quantify the environmental impact of space objects (e.g. [1]) can be used as a mean to rapidly monitor the current state of the environment and of its short to medium term evolution. Of particular concern in this respect are future in-orbit fragmentations which could jeopardize the safety of spacecraft in an increasingly crowded Low Earth Orbit (LEO) space. For an efficient SST network it will be crucial to immediately react to one such catastrophic event both by detecting and characterizing the fragmentation (e.g., [2]) and also by quickly assessing its impact on the other meshes of the chain of services provided by the SST system, such as the collision avoidance.

In this context, building on the definition of the Criticality of Spacecraft Index (CSI) [1] and of the Shell Criticality [3], a procedure and an index able to quantify and visualize the medium term effects on the environment of a fragmentation in Low Earth Orbit can be derived, taking into account the change in the environment caused by the fragmentation of a given mass in a specific orbit. By quantifying the contribution of the fragments with respect to the original situation where the whole fragmented mass was contained in the intact object(s), a first evaluation of the change in the environmental risk can be obtained. As a driving factor, the design philosophy subtended in the definition of the CSI [1] is adopted, i.e., the index shall be quickly analytically calculable with a limited, though sufficient, number of parameters in order to be verifiable and repeatable.

In this work the first derivation of such an index is recalled in Sec. 2., while refined network-related weights are defined in Section 3.. Then, some tests on simulated fragmentations are presented in Sec. 4..

In Sec. 5. a cumulated index, to directly classify and rank different fragmentation events on various regions of LEO, is finally proposed. Finally in Sec. 6. the conclusions are outlined along with a roadmap for future improvements.

2. The Fragmentation Environmental Index

The Fragmentation Environmental Index (FEI), was developed to quantify and visualize, with a simple analytical formulation, the medium term (typically limited to several months after the event) effects on the environment of a fragmentation in Low Earth Orbit (LEO) [4] .The FEI was derived, based on the CSI (Criticality of Spacecraft Index) and the shell indexes developed by the authors in the previous years [1][13][3]. The FEI was developed having in mind the effects on a space surveillance network (SST) of an event creating a large number of fragments. Most of these fragments will be below the current detection threshold of the SST sensors, making these mm and cm-sized objects even more lethal since they won't be trackable and, therefore, not avoidable by the active spacecraft. With this purpose in mind, a multiplicative weight ω_{tr} was introduced in the expression of the CSI (see Eq. (1)) to enhance the importance of the non-trackable objects (e.g., smaller than 10 cm, this threshold being an input of the model) on its computation. The FEI is based on the extension of the Criticality of Spacecraft Index, Ξ, as defined in [13]):

$$\Xi = \frac{M}{M_0} \frac{A}{A_0} \frac{D(h)}{D_0} \frac{L(h)}{L(h_0)} f(i)\omega_{tr}, \qquad (1)$$

where M, A, L are the mass, area and lifetime of the considered object and $D(h)$ is the spatial density around the altitude h where the object is found. $M_0, A_0, D_0, L(h_0)$ are properly defined normalizing factors (see [1] for details).

To get to the FEI, in Eq. (1) the CSI, Ξ, is first multiplied by the above mentioned weighting factor ω_{tr} which satisfies $0 \leq \omega_{tr} \leq 1$, where $\omega_{tr} = 1$ for non-trackable objects and assumes a lower value for trackable objects which depends on the considered surveillance network. Finally the weighted shell index Ξ_{LEO} [3] can be computed pre and post-fragmentation allowing to write the FEI either in terms of absolute difference:

$$\Xi_{FEI} = \Xi_{LEO}(post) - \Xi_{LEO}(pre) \qquad (2)$$

or percentage difference:

$$\Xi_{FEI-PERC} = \frac{\Xi_{LEO}(post) - \Xi_{LEO}(pre)}{\Xi_{LEO}(pre)}. \qquad (3)$$

In [4] it was shown how the FEI is capable of identifying areas in space that have been significantly disturbed due to fragmentation events, without relying on complex long-term population analysis.

However, in [4] the ω_{tr} weighting factor was applied in an heuristic way to the fragment population. In the following section, an improvement of the FEI, using more refined weighting factors is presented. It allows the use of the index to quickly point out regions of space and span of times where a sensor, and the related chain of services (such as collision avoidance), could be stressed by a fragmentation.

3. Improving the FEI

Given the weighting factor introduced in Eq. 1, the index is strongly related to the considered sensor network, in particular to its sensitivity (e.g., expressed in terms of the size of the minimum detectable object at a given altitude). Hence, it is important to understand how a network of sensors is made, and what its components are. In particular, we have to estimate the capabilities of both passive (optical) and active (radar) networks in terms of the sensor's characteristics and to define new weighting factors that will enter the FEI. This can be done by looking for metrics describing the optical and radar detection performances.

3.1 Optical Detection Performance

New optical instruments, having large Field Of Views (typically larger than 5° per aperture), have proven to be particularly suited for high-volume monitoring of orbital debris. Ongoing research, such as [5] aims at optimizing these sensors' integration times, and builds upon this idea to determine the detection performance in various orbital regimes of an optical network.

For our purposes, we can make the simplifying assumption of approximating every fragment to a sphere. In this case, it may be shown that the object's magnitude in the visual band is given by:

$$m_{obj} = m_{sun} - 2.5 \log\left(\frac{s^2}{\rho^2} r p(\Psi)\right) \qquad (4)$$

where s is the size (diameter) of the object, ρ is the range to the object from the observer, r is its reflectance, and $p(\Psi)$ is the solar phase angle function, meaning the angle between the observer and the sun, relative to the fragment. Speaking of r, we will assume for our estimates equal contributions from both its specular and diffuse reflectance components (this is supported by observational data), and we will consider a gray body reflectance for all objects, such that r is constant at all wavelengths. The estimated debris optical albedo r has been recently revised, with recent work by [6] establishing a mean value of $r = 0.175$ for fragmented space debris. The function $p(\Psi)$ is divided in specular phase angle function, $p_{spec}(\Psi)$ and diffuse phase angle function, $p_{diff}(\Psi)$. The former is constant, and its value is $1/4$, while the latter is given by ([5]):

$$p_{diff}(\Psi) = \frac{2}{3\pi}[sin(\Psi) + (\pi - \Psi)cos(\Psi)] \qquad (5)$$

For simplicity, we will always assume $\Psi = \frac{\pi}{2}$, so that:

$$p_{diff}(\Psi) = \frac{2}{3\pi} \qquad (6)$$

is constant. (4) then may be rewritten as:

$$m_{obj} = m_{sun} - 2.5 \log\left[\frac{s^2}{\rho^2}r(\frac{1}{4} + \frac{2}{3\pi})\right] \qquad (7)$$

However, visual magnitudes alone do not allow for a physics-based assessment of sensor performance. Absolute radiometric units, such as irradiance in terms of photon flux (photons/second/area) are required to evaluate passive sensing performance. The conversion is given by (see again [5]):

$$E_{RSO} = 5.6 \times 10^{10} \cdot 10^{-0.4m_{obj}} \qquad (8)$$

and it is measured in $ph/s/m^2$. In the equation above, RSO stands for Resident Space Object. For reference, 20 cm targets at a range of 2000 km are associated with an apparent magnitude of about 12.8 m_v, or irradiance of $\sim 4.2 \times 10^5$ ph/s/m^2. Furthermore, the performance of an optical sensor depends on the angular velocity of an object relative to the ground. When viewed at high elevation angles, lower altitude LEO objects may exceed angular rates of one degree per second, corresponding to 3600 arcsec/s. Telescopes pointing at lower elevation angles are therefore preferred. Moreover, it is known that the volume of observable objects dramatically increases with decreasing elevation angles.
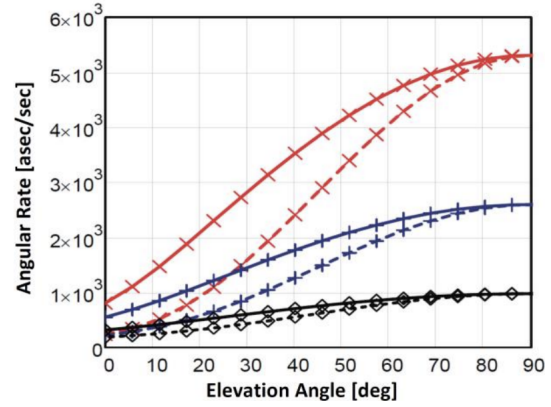

Figure 1: LEO RSO typical angular rates (in arcsec/sec) as seen from the ground, as a function of the telescope's elevation angle. Black, Blue and Red lines represent respectively circular orbits with 300 km, 600 km and 1500 km altitudes. The solid lines represent the maximum angular rate, the dotted lines the minimum. Credits: [5]

The drawback, though, is that the range to a specific object increases with decreasing elevation angle, and so does its apparent magnitude. For instance, objects orbiting in an 800 km altitude orbit are associated with a range of around 1400 km if seen from a ground-based sensor elevated at a 30° angle. In [5] the range of LEO RSO angular velocities as seen from the ground, is plotted as a function of the elevation angle, for different circular orbit altitudes - see Fig. 1. It can be checked that most objects at 300 km altitudes (low LEO) are seen as fast-moving objects: if we assume an elevation of 30°, the corresponding angular speed ranges between 2000 arcsec/sec and 3000 arcsec/sec. At 600 km, the average angular rate goes down and it is seen to take values in the interval 1000 arcsec/sec and 2000 arcsec/sec. The slowest fragments are of course the ones populating the high LEO region: already at around 1500 km, their speed is always below 1000 arcsec/sec. Note that other factors influence the typical pointing directions of a given telescope, depending also on the minimum permitted elevation related to atmospheric disturbances and sensor specifics (e.g., limiting the range of the mounting system).

Angular rates (ARs) and irradiance (E_{RSO}) are important quantities when it comes to space objects detection, because they enter the Signal to Noise Ratio (SNR) equation. Indeed, detecting a fragment is

accomplished by applying a threshold to the counts for each pixel while accounting for known objects and noise contributions. In other words, to detect an object means to look for signals of interest in the noise pattern. In our case, the signal-to-noise ratio provided in terms of photoelectrons per pixel is given by:

$$SNR_{optical} = \frac{e_s}{\sqrt{e_b + e_n^2 + e_{shot}}} \qquad (9)$$

[1] where e_s is the number of signal photoelectrons:

$$e_s = QE \cdot \tau \cdot A \cdot \tau_{atm} \cdot E_{RSO} \cdot t_{sig} \qquad (10)$$

e_b is the number of background photoelectrons:

$$e_b = QE \cdot \tau \cdot L_b \cdot A \cdot \tau_{atm} \cdot \mu^2 \cdot t \qquad (11)$$

and e_n is read noise from the detector in terms of photoelectrons, and e_{shot} is the detection-event-associated shot noise. Shot noise represents the statistical variation of a source's photon emissions over time, and it can be modeled by a Poisson process. We may rewrite (9) as:

$$SNR_{optical} = \frac{QE \cdot \tau \cdot A \cdot \tau_{atm} \cdot E_{RSO} \cdot t_{sig}}{\sqrt{QE \cdot \tau \cdot L_b \cdot A \cdot \tau_{atm} \cdot \mu^2 \cdot t + e_n^2 + e_{shot}}} \qquad (12)$$

In the above equations, QE is the so-called quantum efficiency of the detector, τ and τ_{atm} are the optical and atmospheric transmittance, both responsible of some signal loss, $A = \pi d^2/4$, t_{sig} is the signal integration time (per pixel) of interest, which generally differs from the system integration time t, due to the angular movement of the object during an exposure period. The maximum signal possible is obtained when the fragment moves through the full length of a pixel during an exposure. L_b is the conversion from background signal magnitude to radiometric units:

$$L_b = 5.6 \times 10^{10} \cdot 10^{-0.4m_b} \cdot \left(\frac{180}{\pi}\right)^2 \cdot 3600^2 \qquad (13)$$

where m_b is the surface brightness associated with the background in units of $mag/arcsec^2$. Finally, $\mu = x/f$ is a sensor-related quantity, given by the individual detector size, x, divided by the focal length, f. Recording a detection event thus translates into choosing a suitable threshold for the SNR above which a Resident Space Object can be detected with

a low false alarm rate. As noted in [5], an SNR of six already provides good detection performance.[2] More in general, high SNR thresholds such as the ones required for fragments detection, allow us to reasonably assume a *background-dominated case*, for which $e_b >> e_{shot}, e_n$. Under this assumptions, 12 becomes:

$$SNR_{optical} = \frac{QE \cdot \tau \cdot A \cdot \tau_{atm} \cdot E_{RSO} \cdot t_{sig}}{\sqrt{QE \cdot \tau \cdot L_b \cdot A \cdot \tau_{atm} \cdot \mu^2 \cdot t}} \qquad (14)$$

It is therefore clear that, given a specific sensor with its associated QE, μ, A, t and τ, together with an estimation of the typical τ_{atm}, and considering the suitable case where the background radiance L_b dominates the detector read noise, the $SNR_{optical}$ equation will only depend on the quantities E_{RSO} and t_{sig}:

$$SNR_{optical} \propto E_{RSO} \times \frac{t_{sig}}{\sqrt{t}} \qquad (15)$$

In turn, E_{RSO} ultimately depends on the size of the fragment and the range to the target: $E_{RSO}(s, \rho)$. Assuming a fixed elevation angle for all telescopes, and circular orbits for the targets, it is possible to relate ρ measurements to corresponding LEO altitudes h. Indeed, from the *slant range* equation and solving for h, one gets:

$$h = \sqrt{r_\oplus^2 + \rho^2 - 2r_\oplus\rho\cos(\frac{\pi}{2} + \epsilon_0)} - r_\oplus \qquad (16)$$

ϵ_0 being the elevation angle, $r_\oplus$ being the Earth's radius and ρ the target's slant range. Then we can write $E_{RSO} = E_{RSO}(s, h)$.
On the other hand, t_{sig} can be estimated (as an order of magnitude) to be

$$t_{sig} = \frac{\mu}{AR}, \qquad (17)$$

where AR is the object angular rate with respect to the telescope pointing. Note that this is also the maximum time equal to the transit time through a single pixel on the detector with angular extent μ. If we could take $t = t_{sig}$, we would optimize the $SNR_{optical}$, and have the simpler equation:

$$SNR_{optical} = \sqrt{QE \cdot \tau \cdot A} \frac{\tau_{atm} \cdot E_{RSO}}{\sqrt{L_b \cdot AR \cdot \mu}} \qquad (18)$$

---

[1] Please note that we are neglecting dark noise and other noise sources, as they are assumed to be negligible for modern detectors with the integration times of interest.

[2] An SNR value greater or equal to six is also used in the orbit propagation and observation simulations approach as described in [7], where the efficiency of a network of the new Flyeye telescopes in carrying out HLEO region surveys is addressed.

Altitude (km)	Region
0 < h < 500	low LEO
500 < h < 1000	medium LEO
1000 < h < 2000	high LEO

Table 1: LEO partition in altitude zones

However, this can't be done practically, because it would require an *a priori* knowledge of the debris angular rate, and, in most cases, the object transits more than just one pixel during an exposure. A more realistic estimate is obtained by degrading the optimal $SNR_{optical}$ equation by a factor of $\sqrt{2}$ (see [5]):

$$SNR_{optical} = \frac{1}{\sqrt{2}}\sqrt{QE \cdot \tau \cdot A \frac{\tau_{atm} \cdot E_{RSO}}{\sqrt{L_b \cdot AR \cdot \mu}}} \quad (19)$$

3.1.1 Optical Detectability Function

As discussed above, we can argue that the angular rate of an object roughly depends on its altitude (low LEO, medium LEO, high LEO). Hence, t_{sig} depends on h, $t_{sig} = t_{sig}(h)$, because ultimately $AR = AR(h)$.

Therefore, in this work we define a function of the two parameters size and altitude, $\mathcal{F}(s,h)$:

$$\mathcal{F}(s,h) = A\omega_{E_{RSO}}(s,h) + \omega_{AR}(h) \quad (20)$$

that is a linear combination of two separate weights: one describing the capability of a telescope to detect faint objects, and the other related to how fast the object transits in a given field of view. In the above equation, A is a network-related coefficient.
More specifically, if we subdivide the LEO environment as in Tab. 1, then, referring to the plot in Fig. 1, we can tailor the function $\mathcal{F}(s,h)$ to our network capabilities (i.e. we can assign A a specific value).

For instance, let's assume the ideal case in which the debris cloud is very slow, in terms of angular rate in the sky, as seen by a ground observer. This would lead to a function $\mathcal{F}(s,h)$ which depends only on the observed irradiance of the given fragment while the value of $AR(h)$ is not affecting the performance (all telescopes are assumed to be able to observe a very slow-moving cloud). However, this scenario would not be realistic. Therefore, we assume that only a

few percentage of telescopes is going to be able to observe the fastest fragmentations - i.e. those happening in low-LEO. A realistic network could be characterized by the following: 10% of the network is able to follow fragments moving at angular rates greater or equal than 2000 arcsec/sec; 50% of the network is able to follow fragments with angular rates between 1000 and 2000 arcsec/sec, and 100% of the network is able to follow fragments with angular rates lower than 1000 arcsec/sec (this is also justified by the fact that, according to [8], most telescopes are able to detect objects moving at ~ 1800 arcsec/sec). In other words, the real situation is well described by an exchange between how good the observations are in terms of: 1) object's magnitude - how bright the object appears - and 2) the object's angular rate - how fast it moves relatively to the observer - and the two weights in (20) are intertwined. In this framework, the coefficient A gives us a feeling of the relative importance of the $\omega_{E_{RSO}}$ and ω_{AR} contributions. For a fragmentation happening in low LEO, we set $A = 0.1$, meaning that we give more importance to the latter. This is because we expect a fragment belonging to such a cloud to be the "brightest it can be", but also the "fastest it can be". Applying this reasoning to the other two orbital regimes, we set $A = 0.5$ if the cloud is found in medium LEO, and $A = 1$ for a debris cloud in high LEO. This latter condition also amounts to shutting down the $\omega_{AR}(h)$ contribute for a fragmentation happening in high LEO (see next paragraph). Resuming what we just said, the A coefficient will depend on where in the LEO region the fragmentation has happened, and its value for the three different regimes is given in Tab. 2.

REGION	LOW LEO	MEDIUM LEO	HIGH LEO
A	0.1	0.5	1

Table 2: Value of the A coefficient as it appears in the function $\mathcal{F}(s,h)$.

3.1.2 A New Optical Weight

Once defined the function $\mathcal{F}$, the forms of the two weights entering the equation can be obtained. We start from the assumption of having a number $N_{optical}$ of telescopes, all sharing the same characteristics: every optical sensor can probe the LEO environment up to an altitude h_{max}, say $h_{max} = 2000$

km of altitude, and is able to detect all fragments greater than $s_{min} = 20\ cm$ in size.[3]. Assuming that all telescopes have an elevation of $30°$, the range corresponding to a 2000 km altitude shell is given by the slant range equation (16) and it amounts to $\rho_{max} \sim 3110$ km. The corresponding limit magnitude is given by (4), with $s = 20\ cm$ and $\rho = 3110\ km$. This yields $m_{20,2000} \sim 12.56\ m_v$. This magnitude corresponds to what we can call the *detectability limit* of our network. In the case where we have access to a generic knowledge of the target's range - for instance, given by the first estimates of the orbit coming from the largest observed fragments - we can use Eq. (16) to get the target's altitude, and every fragment smaller than 20 cm at the fragmentation altitude h_{frag} has to satisfy:

$$m_{s_{frag}, h_{frag}} \leq m_{20,2000} \tag{21}$$

where s_{frag} is the fragment size, in order to be detected. Therefore, the first thing to check is for this condition to hold for a given fragment: we won't be able to detect it otherwise. It is important to note that, since the limiting magnitude of a telescope can be approximated by the formula (see [9] for more):

$$m_{lim} = 5\log(D_{lim}) + 7.69, \tag{22}$$

condition (21) sets the diameter (in centimetres) of an average telescope describing our network. In the specific case where $s_{min} = 20$ cm and $h_{max} = 2000$ km:

$$m_{lim} = m_{20,2000} = 12.8 m_v \implies D_{lim} \sim 10cm \tag{23}$$

In practical terms, when we establish a detectability limit for the network, we are essentially describing it as a telescope with a diameter D_{lim}.
Keeping this in mind, let's consider only the fragments we are able to observe and then define the weight:

$$\omega_{E_{RSO}} = 1 - \frac{E_{RSO}(s_{frag}, h_{frag})}{E_{RSO}(s_{min}, h_{frag})} \tag{24}$$

where $s_{min} = 20$ cm and h_{frag} is the altitude of the fragment, assuming it to be on a circular orbit.[4] It is

worth noting the choice of h_{frag} at the denominator, which is needed if we want to have an always-positive weight belonging to the interval $[0, 1]$. Indeed, had we chosen h_{max} in place of h_{frag}, we would have found that observed fragments smaller than s_{min}, at an altitude lower than h_{max}, would be characterized by an E_{RSO} signal *greater* than $E_{s_{min}, h_{max}}$, therefore producing negative weights. We associate the fragments for which condition (21) does not hold with maximum risk, while we give a null weight to fragments bigger or equal to 20 cm in size:

$$\begin{cases} \omega_{E_{RSO}} = 1 - \frac{E_{RSO}(s_{frag}, h_{frag})}{E_{RSO}(s_{min}, h_{frag})}, & \text{if } m_{s_{frag}, h_{frag}} \leq m_{20,2000} \\ \omega_{E_{RSO}} = 1, & \text{if } m_{s_{frag}, h_{frag}} > m_{20,2000} \\ \omega_{E_{RSO}} = 0, & \text{if } s_{frag} \geq 20cm \end{cases}$$

By doing this, we have assigned a weight to the E_{RSO} contribution to the $\mathcal{F}(s, h)$ function, namely $\omega_{E_{RSO}}(s, h)$.
As for $\omega_{AR}(h)$, we make use of the LEO subdivision mentioned above and Fig. 1 and define:

- $AR_{HLEO} \sim 500$ arcsec/sec;

- $AR_{MLEO} \sim 1000$ arcsec/sec;

- $AR_{LLEO} \sim 2000$ arcsec/sec.

The separation into three regions allows us to define the following weight:

$$\begin{cases} \omega_{AR} = 1 - \frac{AR_{HLEO}}{AR_{LLEO}}, & \text{if fragment in low LEO} \\ \omega_{AR} = 1 - \frac{AR_{HLEO}}{AR_{MLEO}}, & \text{if fragment in medium LEO} \\ \omega_{AR} = 0, & \text{if fragment in high LEO} \end{cases}$$

Given the telescope's elevation and diameter, the risk associated with simulated random fragments of various sizes (values of the $\mathcal{F}$ function) can be computed. [5] Figure 2 shows the results for a fragmentation happening in an 800 km and 1000 km altitude shell, respectively. For each plot, there are two size regions for which the associated weight takes either maximum or minimum values.

The former represents the non-visible fragments, i.e. those fragments for which $\omega_{E_{RSO}} = 1$, because they don't satisfy Eq. (21), while the latter is characterized by those fragments greater or equal to s_{min}

---

[3]While this is a useful assumption, it's crucial to emphasize that, as of the present moment, radar sensors exclusively handle tracking below altitudes of 1000 km. The future envisions the utilization of telescopes for surveillance and tracking purposes in low Earth orbit (LEO), but presently, they are primarily utilized for observations in MEO and GEO.

[4]In other words, given the semi-major axis a_{frag}, $h_{frag} = a_{frag} - r_{\oplus}$, with $r_{\oplus} = 6378$ km being the Earth's radius.

[5]Unlike the results we will show later in section **??**, the current fragments **are not** representative of an actual cloud, in the sense that they do not follow a specific mass distribution. We rather generated some sizes in the interval $0 - 20$ cm and plotted the results to have a better grasp on the different weights associated with different fragments.

in size.

In between, there's a whole range of sizes for which $\mathcal{F}(s,h)$ takes values in the interval $[\omega_{min}, \omega_{max}]$. These are seen to be well-fitted by a second-order polynomial (red curve).

A first-order fit showcases generally larger residuals; nevertheless, it might be insightful to display it on the same chart, as a straight line can also be approximated by the simple parametrization:

$$\frac{y - y_1}{x - x_1} = \frac{y_2 - y_1}{x_2 - x_1} \qquad (25)$$

which is the equation of a line passing by two given points, them being: $\left(x_1, y_1\right) = \left(\mathcal{F}(s_{threshold, h_{frag}})\right.$ $\left., s_{threshold}\right)$, with $s_{threshold}$ the size of the smallest detectable fragment capable of producing the lowest detectable signal at the fragmentation altitude h_{frag}, and $\left(x_2, y_2\right) = \left(\mathcal{F}(s_{min, h_{frag}})\,, s_{min}\right)$. While acknowledging the limitations of linear parametrization, it may serve as a tool to provide the operator with a preliminary estimate of the weight associated with a specific fragment, considering the telescope's characteristics, as illustrated in Fig. 2.

In other words, given the optical network specifics and the altitude of the fragmentation (both known), we are able to associate each fragment size with a different value of the optical weight, by means of a simple linear parametrization that takes into account only the minimum detectable fragment at that specific altitude h_{frag}, and the minimum detectable fragment at the maximum altitude h_{max}.

As we will see in the next sections, given an in-orbit fragmentation, it is straightforward to compute the overall risk associated with the debris cloud by summing up the single fragments' contributions to the fractional CSI (Eq. 3).

3.2   Radar Detection Performance

Radar detection of space debris is usually done either via beam park experiments (mainly for space debris environmental studies) or, typically at a lower level of sensitivity, by continuous surveys from the SST sensors. As already done for telescopes, we can describe the radar performance by the following form of the radar range equation, where the ratio between P_S, the signal in the radar receiver, and P_N, the noise signal is considered:

$$SNR_{radar} = P_S/P_N = \frac{P_T G_T G_R \lambda^2}{(4\pi)^3 k T_0 B F_n L} \frac{\sigma}{\rho^4} \qquad (26)$$
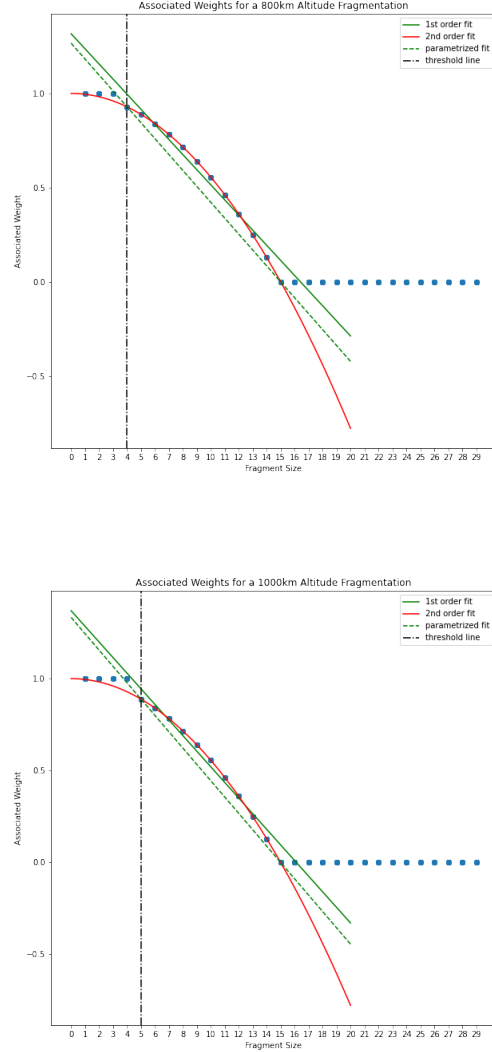

Figure 2: Simulated $\mathcal{F}$ weights for fragments up to 30 cm in two different fragmentation cases happening in an 800 km (top panel) and 1000 km (bottom panel) altitude orbit. The middle part of the plot is well-fitted by a second-order polynomial red line). A first-order fit (green solid line) and the parametrized fit (green dotted line) performed as described above are also displayed.

The interesting dependencies in equation (26) are the ones on the far right, namely the ρ^{-4} and σ terms, where ρ is the object's range and σ is the *radar cross section* (RCS). All other appearing terms constitute the *design parameters*, and they depend

on the specific radar sensors. Here we list them:

- P_T, the *peak transmit power* specified at the output of the transmitter, measured in Watts (W);

- G_T and G_R , transmit and receive antenna transmitting gains. They're both dimensionless;

- λ, the operating radar wavelength in meters (m)

- k, Boltzmann constant, equal to 1.380×10^{-23} $\frac{W}{Hz \cdot K}$

- T_0 , a reference temperature in Kelvin (K), usually set to $T_0 = 290\ K$

- B, the *effective* noise bandwidth of the radar. It is measured in Hertz (Hz).

- F_n , the radar noise figure. It is dimensionless.

- L, a factor that takes into account losses that need to be considered when using the radar range equation, such as the antenna and feed losses.

The RCS, σ, depends on various factors. Among these, the size of the object plays a significant role. Other factors include the material with which the target is made, the size of the target relative to λ, the incident and reflected angle, and the polarization of the radiation (both transmitted and received). Modeling the fragments as isotropic re-emitting spheres of size (diameter) s, and assuming that the ratio $s/\lambda \geq 0.2$ optical regime), the following relation holds [6]:

$$\sigma = \frac{\pi}{4}s^2 \qquad (27)$$

while for smaller ratios (Rayleigh regime) we have:

$$\sigma = \frac{9\pi^5 d^6}{4\lambda^4}s^2 \qquad (28)$$

and the radar cross-section value gives us a hint on the fragment size (see [15]). In other words, considering a radar network described by just one radar with given specifics: $\sigma = \sigma(s)$. We also have $\rho = \rho(h)$, as in the optical case.

3.2.1 A New Radar Weight

Assuming that all radars belonging to the network are able to detect $s_{min} = 15\ cm$ sized objects up to an altitude of $h_{max} = 1200\ km$ [7], we can:

- compute the corresponding expected Signal to Noise Ratio for a given fragment of size s_{frag} at a given fragmentation altitude h_{frag}, $SNR_{radar}(s_{frag}, h_{frag})$;

- address its detectability, meaning check whether:

$$SNR_{radar}(s_{frag}, h_{frag}) > SNR_{radar}(s_{min}, h_{max}) \qquad (29)$$

- in case the inequality holds true, compute the weight:

$$\omega_{radar} = 1 - \frac{SNR_{radar}(s_{frag}, h_{frag})}{SNR_{radar}(s_{min}, h_{frag})} \qquad (30)$$

this is somehow analogous to the procedure presented in the optical case, where we stress the dependence on h_{frag} at the denominator, so as to ensure that $w_{radar} \in [0, 1]$.

As done earlier with the telescope case, we wrote a Python script to compute the radar weight associated with each fragment size, which is shown in Fig 3. Here, it is assumed that all radar sensors observe at a 30° elevation and that $s_{min,radar}$ - sized objects are detectable at a given altitude of $h_{max,radar}$. Considering all other quantities in the radar SNR equation as constant, this amount to give a specific value for G_T and G_R. More specifically, the product of these two quantities gives a practical description of a sensor representing the network.

4. Simulations and results

To test the new index formulation, we simulated a collision between a 2000 kg upper stage (parent object) with orbital elements: $(a_p, e_p, i_p) = (8178\ km, 0.00003, 80.3°)$ and a 15 kg piece of debris, with a relative velocity of 10 km/s. Due to the size and velocity of the projectile, the collision leads to a complete fragmentation of the target. The resulting debris cloud was propagated up to a time $t_{end} = 100$

---

[6]This is true for a wide range of applications. For instance, taking $s_{min} = 5\ cm$, the $s/\lambda \geq 0.2$ ratio condition holds true for Ka, Ku, X, C, S, and part of the L band.

[7]Similarly to what we have already mentioned in 3, we stress that radar sensors are mostly employed to observe altitude shells up to 1000 km, as they suffer from rapid SNR degradation at higher altitudes ($SNR_{radar}\ \alpha\ \rho^{-4}$) .
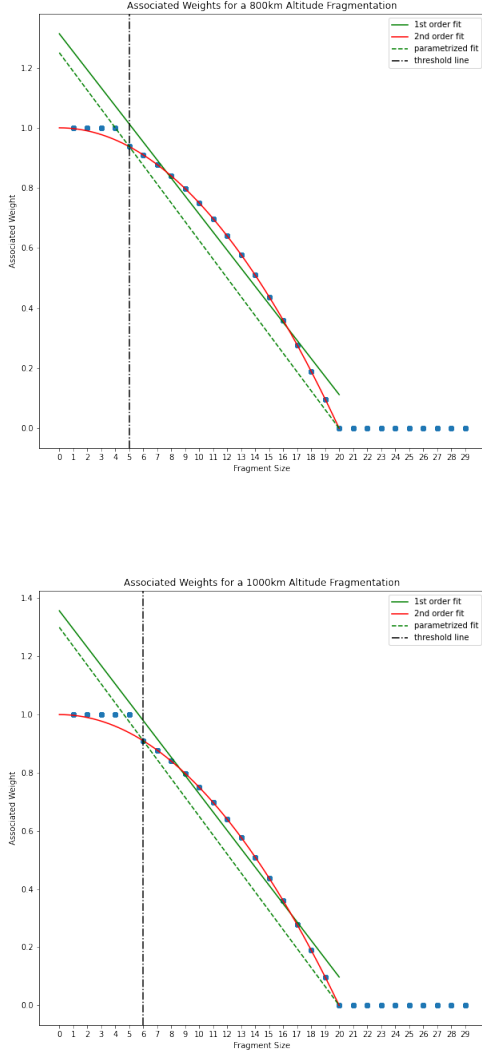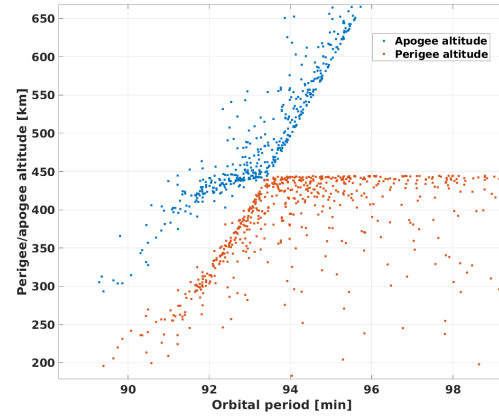
radars to probe the Low Earth Orbit (LEO) environment up to 1200 km in altitude, and telescopes to detect objects at altitudes higher than 1200 km. In accordance with the definition of ω_{AR}, this implies setting $\omega_{AR} = 0$ for our simulations. This division between radar vs optical regime reflects the current routine of the SST services. Indeed, radars demonstrate superior performances compared to telescopes at lower Low Earth Orbit (LEO) altitudes. However, their effectiveness is constrained by a limited range, as indicated by the relationship $SNR_{radar} \propto \rho^{-4}$. On the other hand, optical telescopes offer a cost-effective alternative for higher altitudes, where the use of very powerful (hence expensive) radars would be necessary.

4.1   450 km Altitude Fragmentation

The Gabbard Diagram of the 450 km altitude fragmentation is shown in Fig. 4. Since we have $h_{frag} = 450km < 1200\ km$, we consider a pure radar network to be in place, with all sensors pointing at an elevation angle of 30°. The minimum detectable size, s_{min} of a fragment at a given altitude h_{max} can be taken as a proxy for the network's capabilities. We considered, respectively: $s_{min} = 15$ cm, 10 cm, 5 cm at $h_{max} = 1200$ km for radar sensors. [8]

Figure 3: Simulated ω_{radar} weights for fragments up to 30 cm in two different fragmentation cases happening in an 800 km (top panel) and 1000 km (bottom panel) altitude orbit. A first-order fit (green solid line) and the parametrized fit (green dotted line) performed as described above are also displayed.

Figure 4: Gabbard diagram associated with the $h_{frag} = 450$ km fragmentation.

days. We conducted simulations for four different fragmentation altitudes: $h_{frag} = 450$ km, 800 km, 1200 km, and 1800 km. For sake of conciseness, we only present and analyze in detail the results obtained for $h_{frag} = 450$ km and $h_{frag} = 1200$ km. For our study, we chose to model a network employing

---

[8]These values may represent the capabilities of currently deployed radars used by various entities and companies worldwide for space surveillance and tracking. However, our code allows users to customize this choice for testing any specific network.
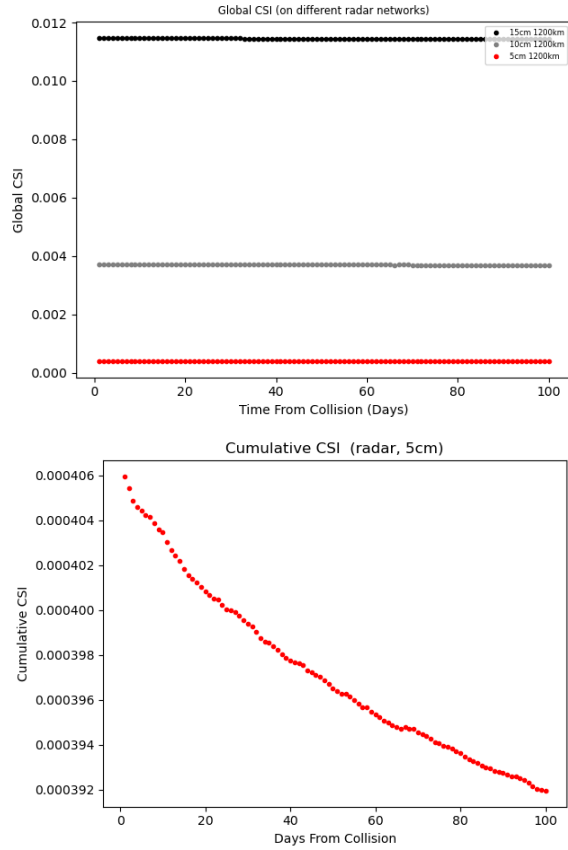
Figure 5: Global CSI associated with a $h_{frag} = 450$ km fragmentation as a function of time, for different radar networks (top panel). The bottom panel shows only the $s_{min} = 5$ cm case to highlight the decrasing trend.

4.1.1 Global CSI

In the top panel of Fig. 5 we show the computed effect of different networks on the computation of the overall LEO CSI (Global CSI) value as a function of time. This value decreases as the capability of the network increases, transitioning from radars with $s_{min} = 15$ cm to a network characterized by $s_{min} = 5$ cm. At first glance, it might seem like the Global CSI values remain constant over time. However, a closer inspection shows how they monotonically decrease over time, due to the decaying of the fragments over time, caused by the atmospheric drag, given the low altitude of this event as seen in the bottom panel of Fig. 5, which is a zoom-in on the red curve in 5 for the $s_{min} = 5$ cm curve. The improvement provided by the network with $s_{min} = 5$

cm over the one with $s_{min} = 15$ cm is visually captured by Fig. 6, showing that the $s_{min} = 5$ cm radar network produces a CSI that is approximately $96\% - 97\%$ lower than the $s_{min} = 15$ cm network.
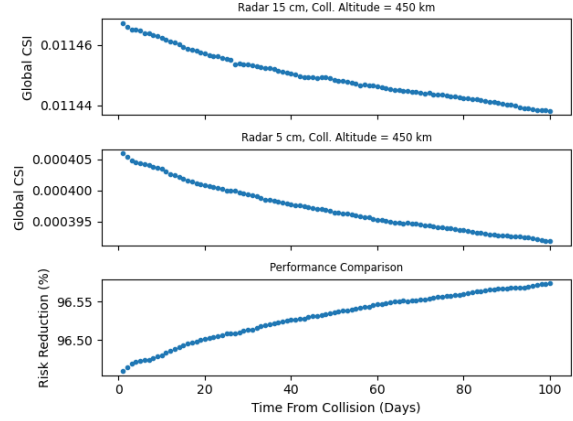

Figure 6: Comparison of Global CSI values as given by two different networks. Top: network with $s_{min} = 15$ cm; middle: network with $s_{min} = 5$ cm; bottom: percentage ratios between the two produced CSIs.

4.1.2 Cloud CSI

It is also interesting to take a look at the cloud's contribution to the Global CSI described in the previous section. In Fig. 7 the cloud contributions for the three different networks are compared. For reference, we also plot (blue dots) the cloud's CSI values in the scenario where no fragment is detectable (i.e., the blue dots correspond to the case where all fragments have $w_{radar} = 1$). From Fig. 7, it is evident that an improvement in network capability results in a reduction in the Cloud's CSI value. It is noteworthy that, with the advancement of the network, the cloud's influence on Global CSI becomes more significant. This is demonstrated in Fig. 8, where we observe approximately a 6% contribution of the clouds to the overall Low Earth Orbit (LEO) criticality in the case of a radar network described by $s_{min} = 5$ cm, one day after the fragmentation epoch. In contrast, contributions for other networks consistently remain below this percentage value, approximately 1% at $s_{min} = 10$ cm and around 0.5% at $s_{min} = 10$ cm. This can be explained by the fact that a more advanced network is more sensitive to changes in the environment, making a specific cloud
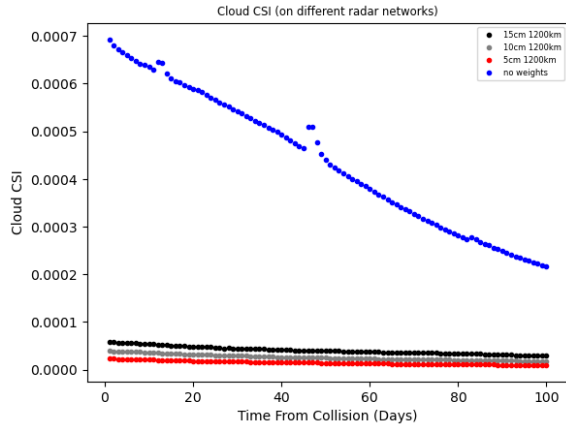
Figure 7: Cloud's CSI contribution as computed using weights associated to different radar networks. The blue dots correspond to the case in which no network is in place, and all fragments are associated with a maximum weight of 1.

more noticeable. Further support for this explanation comes from noticing how the cloud's contribution to the Global CSI is nearly zero in the case when $w_{radar} = 1$ (represented by the blue dots). In this scenario, the CSI associated with the background is very high, and the cloud's contribution becomes almost indistinguishable within it.
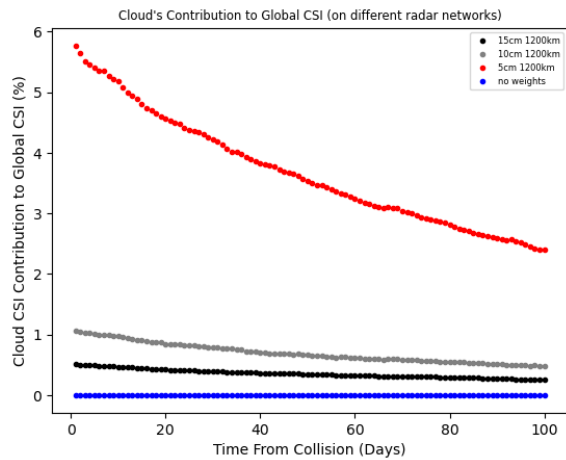
Figure 8: Debris cloud's contribution to the global CSI, for different networks. The blue dots correspond to the case where the same maximum weight of 1 is assigned to all fragments.

4.1.3 FEI

The results of the computation of the FEI, performed as discussed in Sec. 2. an 3., are shown in Figs. 9 and 10. The first plot displays the percentage FEI given by (3) on the $s_{min} = 5\ cm$ network, respectively at 1 (solid line) and 100 days (dotted line) after the fragmentation event. Although the percentage FEI effectively identifies altitudes experiencing significant stress from fragmentation, it lacks the ability to convey the magnitude of the difference between pre-and post-fragmentation. It is possible for two distinct fragmentations, characterized by different values of Ξ_{pre} and Ξ_{post}, to result in the same $\Xi_{FEI-PERC}$ ratio. This similarity arises because the denominator serves as a normalization factor, preventing a clear understanding of the magnitude of the numerator. In order to solve this degeneracy, we also compute the values of Ξ_{FEI} as in Eq. (2) and plot them in top panel of Fig. 10. In this plot, it is evident that the lowest LEO shells are characterized by a very low FEI, indicating that the difference between the post-fragmentation and pre-fragmentation situations is very small. By multiplying the two functions $\Xi_{FEI-PERC}$ and Ξ_{FEI}, to keep track of the magnitude of the FEI as defined by the differences only, we obtain the plot shown in the bottom panel of Fig. 10, which shows a prominent bump corresponding to the relevant fragmentation altitude. All three images provide an insight into how the FEI evolves over time.

A robust environmental index should also effectively capture the overall risk at a specific time, essentially tracking the cloud as it propagates and spreads within the LEO region. Observing the Modulated FEI plot in the bottom panel of Fig. 10, the impact of atmospheric drag, which acts as a sink for all the fragments, is clearly visible.

4.2 1200 km Altitude Fragmentation

We now move to the fragmentation happening at our assumed radar observation limit[9], characterized by $h_{frag} = 1200\ km$. At this regime, we switch to an optical network. Three different optical networks, characterized by $s_{min} = 20\ cm,\ 15\ cm,\ 5\ cm$ at a maximum altitude of $h_{max} = 2000$ km have been tested. All telescopes are assumed to have a 30°

---

[9]We remember that the limiting altitude is a model parameter and we note that in the operational environment within, e.g., the US surveillance network, very powerful radars are used even above this 1200 km limit, used here as a test value.
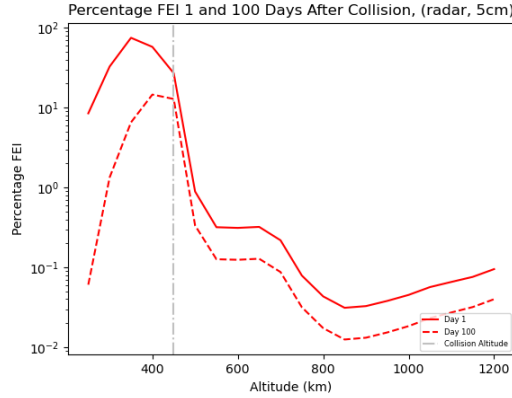
Figure 9: Percentage FEI as computed on a network characterized by $s_{min} = 5\ cm$ at an altitude of $h_{frag} = 450\ km$

elevation.

4.2.1 Global CSI

As observed in the two panel of Fig. 11, the influence of various networks on the overall CSI evolves similarly to what we have previously discussed for the 450 km fragmentation. The global CSI value decreases as the network's sensitivity increases, transitioning from telescopes with $s_{min} = 20$ cm to a network characterized by $s_{min} = 5$ cm. The bottom panel of Fig. 11 specifically highlights this behavior for the network with $s_{min} = 5$ cm, and analogous patterns emerge for the remaining two networks. The Cumulative Cloud CSI plot is remarkably different from the one previously shown for a $450\ km$ fragmentation, as a small increase (of the order $\sim 10^{-5}$) can be observed in the cloud's CSI up to 40 days after the fragmentation epoch. The behavior depicted in the bottom panel of Fig 11 is most likely a consequence of the complicated interplay between 1) the breakup model used and 2) the evolutionary dynamics of fragments spreading the cloud of fragments over different altitude bands. The enhanced performance of the $s_{min} = 5$ cm telescope network is again visually captured in Fig. 12, indicating a CSI approximately 95% lower than the $s_{min} = 20\ cm$ network.

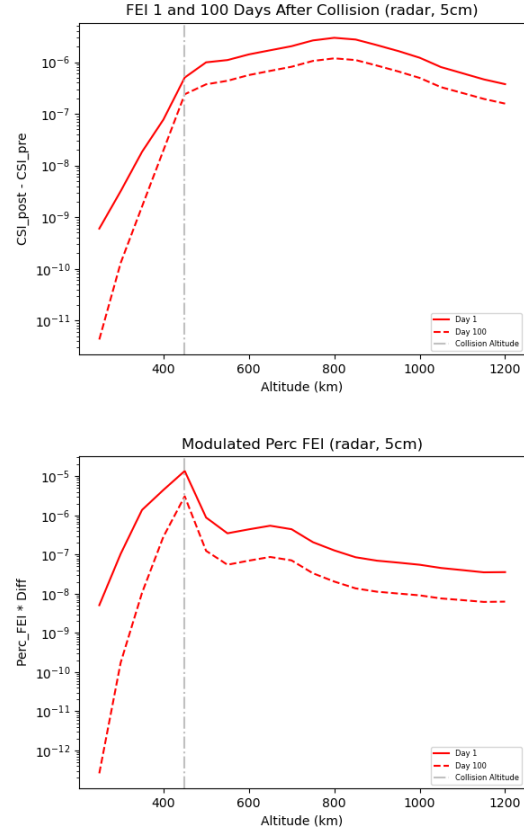Figure 10: Top panel: FEI as computed on a network characterized by $s_{min} = 5\ cm$ at an altitude of $h_{frag} = 450\ km$. Bottom panel: plot showing the product between the FEI and the Percentage FEI values, as computed on a network characterized by $s_{min} = 5\ cm$ at an altitude of $h_{frag} = 450\ km$.

4.2.2 Cloud CSI

The plots depicting the CSI evolution exhibit a general pattern consistent with those previously presented for the $h_{frag} = 450$ km fragmentation. The highest Cloud's CSI values are observed when all fragments are given equal weight ($w_{tr} = 1$), decreasing as the optical network's performance improves (see Fig. 13). However, the most intriguing result is illustrated in Fig. 14. Notably, the $s_{min} = 5$ cm optical network demonstrates remarkable sensitivity, with the cloud accounting for a significant 70% of the globally computed CSI. In contrast, lower values of $10\% - 15\%$ are observed for less powerful networks, with the percentage decreasing as the sensor's capability diminishes.
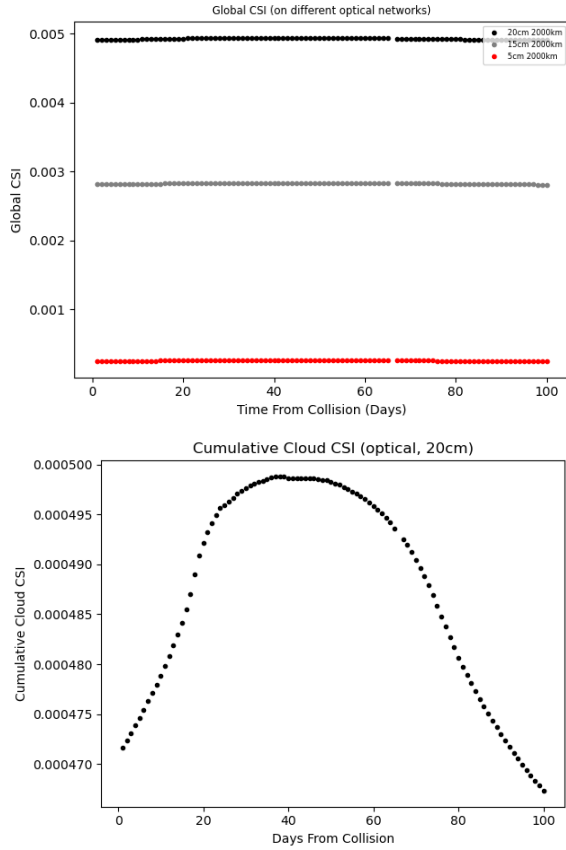
Figure 12: Comparison of Global CSI values as given by two different optical networks. Top: network with $s_{min} = 20$ cm; middle: network with $s_{min} = 5$ cm; bottom: percentage ratios between the two produced CSIs shown in the top panels.

Figure 11: Top panel: Global CSI associated with a $h_{frag} = 1200$ km fragmentation as a function of time, for different optical networks. Bottom panel: detail for the $s_{min} = 5$ case (black line in the top panel).

4.2.3 FEI

The FEI plots (Figs. 15, 16, 17) showcase once again the ability of the index to localize the altitude shells that are mostly interested by a fragmentation (in this case, $h_{frag} = 1200$ km). The atmospheric drag effect at high altitudes is not present. For this reason, no relevant change in the FEI is observed at day 100 with respect to day 1.

We obtained similar plots for the fragmentations at $h_{frag} = 800$ km and $h_{frag} = 1800$ km. Given that they basically share the same trends and show the same results as the two already discussed cases, it is not considered necessary to present them here.

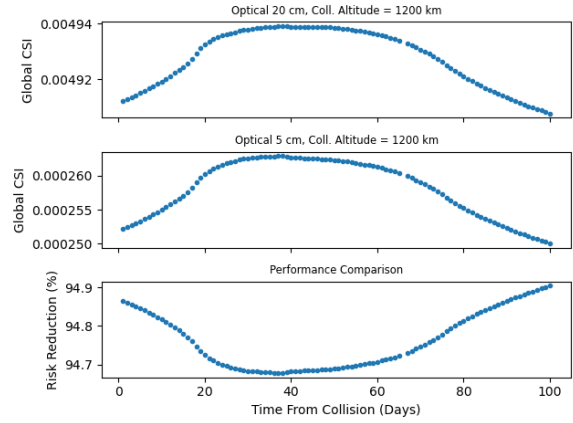In conclusion, our results show how the improved FEI can be used to characterize the effects on the space environment of a fragmentation, leveraged by the performances of a given network of sensors. Additionally, it identifies specific altitude shells that are expected to be particularly affected by the debris cloud in the short term.

5. A cumulative index for fragmentation ranking

On the same line of what is done in [3], by summing up the weighted CSI for all the fragments in a debris cloud it is possible to obtain a cumulative index which, once properly normalized, can give a ranking of the danger represented by a given fragmentation leveraged by the observing capabilities of the underlying SST network. The two panels of Figure 18 show the cumulated CSI for the fragmentation at 450 km (top), as observed by a radar network, and at 1200 km, observed by an optical network. The index values are cumulated over 100 days and are normalized by the cumulated value obtained for a network capability of 15 cm at $h_{max} = 1200$ km for radar and $h_{max} = 2000$ km for optical sensors.

By properly parametrizing a given network, the cumulated index can provide an immediate ranking of a fragmentation event with respect to a "standard" event, thus rapidly informing the SST system of the severity of the event.
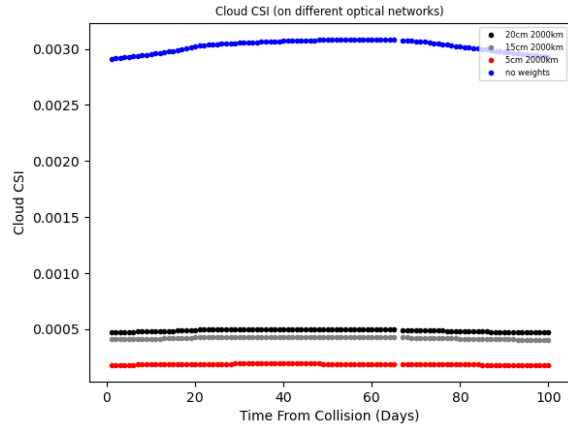
Figure 13: Cloud's CSI contribution as computed using weights associated to different optical networks. The blue dots correspond to the case in which all fragments are associated with a maximum weight of 1.
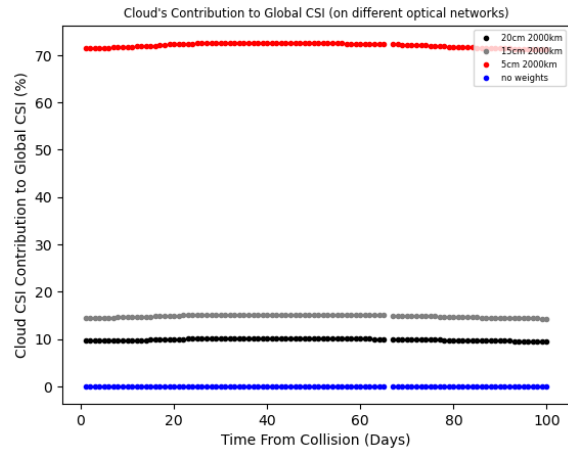

Figure 15: Percentage FEI as computed on a network characterized by $s_{min} = 20\ cm$ at an altitude of $h_{frag} = 1200\ km$

Figure 14: Cloud's contribution to the global CSI, for different networks. The blue dots correspond to the case where the same maximum weight of 1 is assigned to all fragments.

6. Conclusions and future work

Exploiting the criticality index, previously developed by the authors in [1], a new index, dubbed FEI, to characterize the effects on the environment of a fragmentation event was devised in [4]. The focus of the FEI index is to highlight the impact of a given fragmentation on a space surveillance system. This is done by introducing specific weighting factors to inc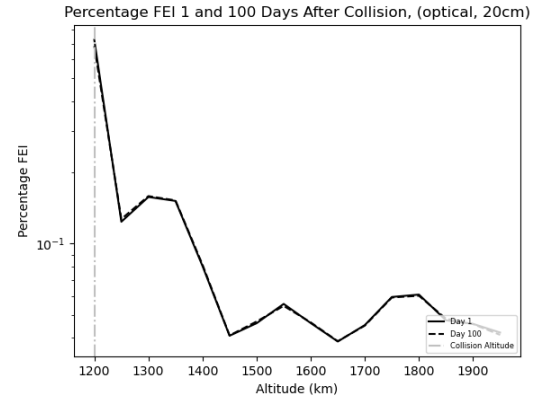rease the importance, in the index computation, of objects not visible from the considered network of sensors. While in [4] the weighting factors were introduced *ad hoc*, in this work a thorough analysis of the observability of small fragments, given the characteristics of the available SST network (either optical or radar), is presented, leading to new improved weights.

The results for a few simulated fragmentations show that the index is capable of characterizing the evolution of the fragment clouds and their impact on the environment around the event location. Moreover, the risk associated to a given fragmentation cloud is leveraged with the capabilities of a specific observation network. This can provide also an information on the stress posed by the fragmentation event on a given SST system and on the capability of the system to properly monitor the event.

By summing up the weighted CSI for all the fragments within a cloud and by normalizing the resulting values with respect to a reference network performance, a cumulated index over a specific time span can be used to directly classify and rank different fragmentation events on different regions of LEO.

Further work is planned for the extension of the index for other regions of the circumterrestrial space, above LEO. This entails also additional considerations on the formulation of the CSI index, especially for what concerns the lifetime terms, $\mathcal{L}$, in Eq. 1.
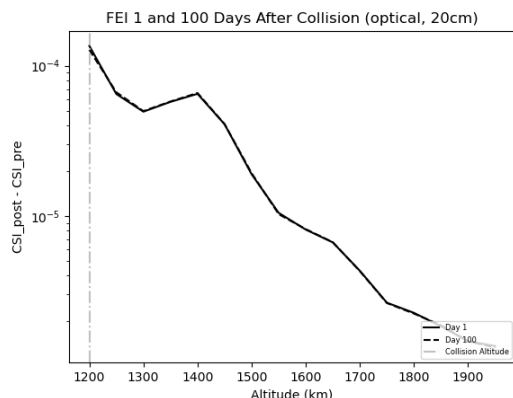
Figure 16: FEI as computed on a network characterized by $s_{min} = 20\ cm$ at an altitude of $h_{frag} = 1200\ km$.
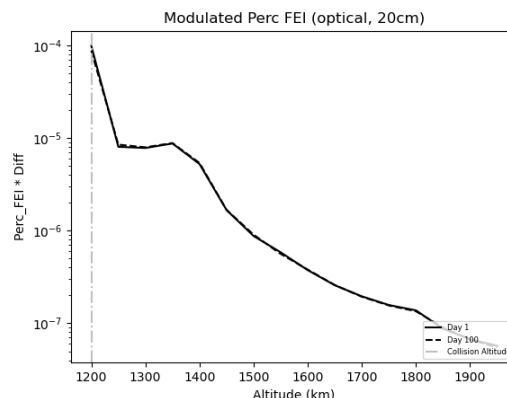

Figure 17: Plot showing the product between the FEI and the Percentage FEI values, as computed on a network characterized by $s_{min} = 20\ cm$ at an altitude of $h_{frag} = 1200\ km$.

2023-2025".

References

[1] Rossi A., G.B. Valsecchi and E.M. Alessi, The Criticality of Spacecraft Index, *Advances in Space Research*, 56, 449-460 (2015)

[2] Di Mare L., S. Cicalò, A. Rossi, E.M. Alessi, G.B. Valsecchi, In-orbit fragmentation characterization and parent bodies identification by means of orbital distances, In *First International Orbital Debris Conference*, 9-12 December, 2019, Sugar Land, Texas (2019)

[3] Bombardelli C., E.M. Alessi, A. Rossi and G.B. Valsecchi, Environmental effect of space debris repositioning, *Advances in Space Research*, 60 (1), 28-37 (2017)

[4] Rossi A., E. Vellutini, E. Alessi, G. Schettino, V. Ruch, and J. Dolado Perez, Environmental index for fragmentation impact and environment evolution analysis, *Journal of Space Safety Engineering*, vol. 9, no. 2, pp. 269-273 (2022)

[5] Shell J., Optimizing Orbital Debris Monitoring with Optical Telescopes, in *Proceedings of the Advanced Maui Optical and Space Surveillance Technologies Conference*, Sep. 2010.

[6] Mulrooney M., M. Matney, M. Hejduk, and E. Barker, An Investigation of Global Albedo Values, Jan. 2008.

[7] Pellegrini R., P. Gregori, F. Cerutti, L. Dimare, F. Bernardi, D. Bracali Cioci, and E. Vellutini, SUTED4L -Study for the application of the Flyeye Telescope to the Survey of the High-LEO orbital region, in *2nd NEO and Debris Detection Conference. Darmstadt*, Germany, ESA Space Safety Programme Office, Jan. 2023.

[8] Yurasov V. and V. Shargorodskiy, Features of space debris survey in LEO utilizing optical sensors, *Proc. 5th European Conference on Space Debris*, Darmstadt, Germany, 30 March - 2 April 2009, (ESA SP-672, July 2009)

[9] Crumey A., Human contrast threshold and astronomical visibility, *Monthly Notices of the Royal Astronomical Society*, vol. 442, no. 3, pp. 2600-2619, Aug. 2014.

[10] Mc Knight D., R. Witner, F. Letizia, S. Lemmens, L. Anselmo, C. Pardini, A. Rossi, C. Kunstadter, S. Kawamoto, V. Aslanov, J-C. Dolado Perez, V. Ruch, H. Lewis, M. Nicolls, L. Jing, S. Dan, W. Dongfang, A. Baranov, D. Grishko, Identifying the 50 statistically most concerning derelict objects in LEO, *Acta Astronautica*, 181, 282-291 https://doi.org/10.1016/j.actaastro.2021.01.021 (2021)

[11] Johnson, N.L., Krisko, P.H., Liou, J.C., Anz-Meador, P.D., NASA's New Breakup Model of EVOLVE 4.0, *Adv. Space Res.*, 28 (9), 1377-1384 (2001).

[12] Rossi, A., Anselmo, L., Pardini, C., Jehn, R., Valsecchi, G. B., The new space debris mitigation (SDM 4.0) long term evolution code, *Proceedings of the Fifth European Conference on Space Debris*, Darmstadt, Germany, Paper ESA SP-672 (2009)
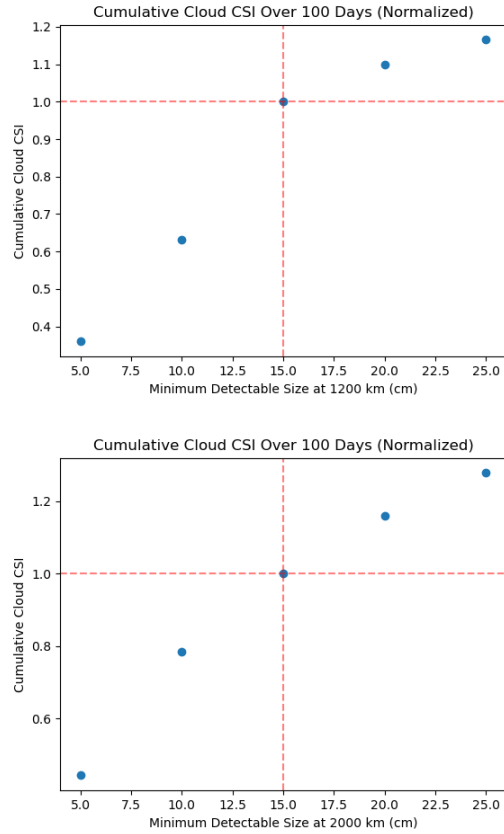
Figure 18: Top panel: weighted CSI cumulated over 100 days, associated with a $h_{frag} = 450\ km$ fragmentation, as a function of the radar network sensitivity. Bottom panel: the same as in the top panel, for a fragmentation at $h_{frag} = 1200\ km$ observed by an optical network with different sensitivity.

[13] Rossi A., E.M. Alessi, G.B. Valsecchi, H. Lewis, J. Radtke, C. Bombardelli, B. Bastida Virgili, A Quantitative Evaluation of the Environmental Impact of the Mega Constellations, *Proceedings of the 7th European Conference on Space Debris*, ESOC, Darmstadt (Germany), 18-21/04/2017 (2017)

[14] Rossi A., Petit A., McKnight D., Short-term space safety analysis of LEO constellations and clusters, *Acta Astronautica,* 175, 476-483, https://doi.org/10.1016/j.actaastro.2020.06.016 (2020)

[15] G. Mie, Beiträge zur Optik trüber Medien, speziell kolloidaler Metallösungen, *Annalen der Physik,* vol. 330, Issue 3, pp.377-445 https://doi.org/10.1002/andp.19083300302)